frontiers in Chemical Engineering

ORIGINAL RESEARCH
published: 28 April 2021
doi: 10.3389/fceng.2021.650301

Ce-Doped PANI/Fe_3O_4 Nanocomposites: Electrode Materials for Supercapattery

Subash Pandey[1,2], *Shova Neupane*[2]*, *Dipak Kumar Gupta*[1,2], *Anju Kumari Das*[2], *Nabin Karki*[2], *Sanjay Singh*[2], *Ram Jeewan Yadav*[3] *and Amar Prasad Yadav*[2]*

[1] Department of Chemistry, Tri-Chandra Multiple Campus, Tribhuvan University, Kathmandu, Nepal, [2] Central Department of Chemistry, Tribhuvan University, Kirtipur, Nepal, [3] Department of Chemistry, Prithvi Narayan Campus, Tribhuvan University, Pokhara, Nepal

In this study, we report on a combined approach to preparing an active electrode material for supercapattery application by making nanocomposites of Polyaniline/Cerium (PANI/Ce) with different weight percentages of magnetite (Fe_3O_4). Fourier-transform infrared spectroscopy (FTIR) and x-ray diffraction (XRD) analyses supported the interaction of PANI with Ce and the formation of the successful nanocomposite with magnetite nanoparticles. Scanning electron microscopy (SEM) and transmission electron microscopy (TEM) analyses showed the uniform and porous morphology of the composites. Cyclic voltammetry (CV) and galvanostatic charge–discharge (GCD) were used to test the supercapattery behavior of the nanocomposite electrodes in 1.0 M H_2SO_4. It was found that the supercapattery electrode of PANI/Ce+7 wt.% Fe_3O_4 exhibited a specific capacity of 171 $mAhg^{-1}$ in the potential range of −0.2 to 1.0 V at the current density of 2.5 Ag^{-1}. Moreover, PANI/Ce+7 wt.% Fe_3O_4 revealed a power density of 376.6 Wkg^{-1} along with a maximum energy density of 25.4 $Whkg^{-1}$ at 2.5 Ag^{-1}. Further, the cyclic stability of PANI/Ce+7 wt.% Fe_3O_4 was found to be 96.0% after 5,000 cycles. The obtained results suggested that the PANI/Ce+Fe_3O_4 nanocomposite could be a promising electrode material candidate for high-performance supercapattery applications.

Keywords: Ce-doping, magnetite nanocomposites, polyaniline, specific capacity, supercapattery

OPEN ACCESS

Edited by:
Richard G. A. Wills, University of Southampton, United Kingdom

Reviewed by:
Ramesh Kasi, University of Malaya, Malaysia
Luis Fernando Arenas, University of Southampton, United Kingdom

***Correspondence:**
Shova Neupane
shova_n@yahoo.com
Amar Prasad Yadav
amar2y@yahoo.com

Specialty section:
This article was submitted to Electrochemical Engineering, a section of the journal Frontiers in Chemical Engineering

Received: *06 January 2021*
Accepted: *29 March 2021*
Published: *28 April 2021*

Citation:
Pandey S, Neupane S, Gupta DK, Das AK, Karki N, Singh S, Yadav RJ and Yadav AP (2021) Ce-Doped PANI/Fe_3O_4 Nanocomposites: Electrode Materials for Supercapattery. Front. Chem. Eng. 3:650301. doi: 10.3389/fceng.2021.650301

INTRODUCTION

The study of energy storage devices is an important field of research aiming to develop the next generation of cost-effective, durable, energy-efficient, and environmentally friendly power sources for the feasible implantation of renewable energy (Patil et al., 2011). Electrochemical capacitors are a family of energy storage devices possessing excellent reversibility, high power delivery or uptake ability, and long operating lifetimes due to either the high reversible ion adsorption mechanism or the fast surface redox reaction (Simon and Gogotsi, 2008; Salanne et al., 2016; Wang et al., 2017). These remarkable features make electrochemical capacitors promising devices for power capture and supply, backup, safety, and low-maintenance applications (Hall et al., 2010). The low energy density (E) of electrochemical capacitors can be enhanced by hybridizing their merits with battery-grade materials together in a single device (Yu and Chen, 2020).

Supercapattery, a supercapacitor mixed with a battery, takes the merits of the high charge–discharge capability of supercapacitors and the large charge storage ability of batteries

(Yu and Chen, 2016). In electrical double-layer capacitors (EDLCs), the capacitance arises by the accumulation of charges at the electrode/electrolyte interfaces on the application of voltage bias (Ji et al., 2014). In pseudocapacitors (PCs), the pseudocapacitance arises from superficial faradic reaction occurring at the electrode/electrolyte interfaces and possesses a much higher specific capacitance (Hu et al., 2015). Transition metal compounds (oxides/hydroxides/nitrides/sulfides) and electronically conducting polymers are extensively researched active materials for usage in PCs (Ballarin et al., 2019). The electrode materials in batteries store faradic charge but are non-capacitive in nature, which results in peak-shaped cyclic voltammetry (CV) and a non-linear galvanostatic charge–discharge (GCD) curve (Yu and Chen, 2016). The metal oxides and conducting polymer composites as redox materials can play an important role in the charge storage of a supercapattery (supercapacitor + battery) cells. These composites gained the merits of both capacitive and non-capacitive faradic charge storage mechanisms (Ma et al., 2013).

Among several electronically conducting polymers, polyaniline (PANI) has gained particular interest for its excellent redox reversibility, superior capacitive behavior with a high specific capacity, low cost, facile synthesis in the form of powder or thin-film by chemical or electrochemical oxidative polymerization, environmental-friendliness, and unique doping/dedoping behaviors (Li et al., 2009; Jiang et al., 2014). Despite all these peculiar features, one of the challenging issues that render PANI an active material for high-performance supercapattery is its low electronic conductivity and poor stability during the charge–discharge process (Patil et al., 2012; Tharani and Vinayagam, 2015). Extensive research work has been carried out to overcome this issue. An approach to tackle this issue is either metal doping, which enhances the electronic conduction of the electrode, or metal oxide nanocomposite formation, which facilitates the diffusion of ions due to the large accessible internal surface area. The latter provides an enhanced charge–discharge rate and, hence, supercapattery performance (Patil et al., 2012; Zeng et al., 2016).

In recent years, the doping of f-block Ce has gained more attention. It is due to the higher stability stemming from the accessibility of the shielded 4f orbitals for strong binding affinity with the nitrogen lone pair of PANI and the suitable redox activity (Tharani and Vinayagam, 2015; Li et al., 2018). Of the metal compounds, spinel metal oxides Fe_3O_4 nanoparticles have received more considerable attention. It has added merits such as improving the electrochemical activities, inexpensiveness, high theoretical specific capacity (926 $mAhg^{-1}$), large potential window, and environmental compatibility (Umare et al., 2010; Xavier et al., 2014; Nithya and Arul, 2016; Prasankumar et al., 2018). Li et al. prepared PANI/Ce^{3+} and PANI/Ce^{4+} composites by *in situ* polymerization and found that the electrical conductivity of PANI/$Ce(NO_3)_3$ increased by 377% in comparison to pure PANI. The result was attributed to more charges and faster movements of Ce^{3+} (Li et al., 2018). Rantho et al. fabricated symmetric supercapacitors with supercapattery behavior based on carbonized iron cations adsorbed onto polyaniline, which exhibited a higher energy and power density of 41.3 $Whkg^{-1}$ and 231.9 Wkg^{-1}, respectively (Rantho et al., 2018). Prasankumar et al. investigated the pseudocapacitive performance of PANI wrapped over Fe_3O_4 nanoparticles and found that voids are built during the formation of microspheres from the nanosphere, which improved the charge storage (Prasankumar et al., 2018). A capacitance value of 572 Fg^{-1} at 0.5 Ag^{-1} was reported with capacitance retention of 82% after 5,000 charge–discharge cycles. Although the porous PANI/Fe_3O_4 nanocomposites used in the study enhanced the capacitive performance of the supercapacitors, the rate performance data implied limited ion transport and ion accessibility.

Herein, nanocomposites based on different weight percentages of Fe_3O_4 nanoparticles encapsulated in Ce-doped PANI were prepared by *in situ* chemical oxidative polymerization and used as active materials to prepare electrodes for high-performance supercapattery. The objective of the synthesis of PANI/Ce+7 wt.% Fe_3O_4 nanocomposite electrode for supercapattery is to improve the electronic conductivity by doping along with an increase in charge–discharge rate due to a decrease in the diffusion path length by the formation of nanocomposites. The Fe_3O_4 nanoparticle concentration was varied to determine its effect on the magnitude of different electrochemical performance metrics of PANI/Ce.

MATERIALS AND METHODS

Materials

Aniline, obtained from Fisher Scientific, India, was purified using the double distillation method under reduced pressure. Ammonium persulfate ($[NH_4]_2S_2O_8$) and Cerium (III) nitrate hexahydrate ($Ce[NO_3]_3.6H_2O$) were obtained from SD Fine Chemicals, India. Ammonium iron (II) sulfate hexahydrate ($[NH_4]_2Fe[SO_4]_2.6H_2O$), iron(III) chloride hexahydrate ($FeCl_3.6H_2O$), sulfuric acid (H_2SO_4), sodium hydroxide (NaOH), hydrochloric acid (HCl), and Cetrimide purified were obtained from Merck Life Science Private Ltd., India. The binder polyvinylidene difluoride (PVDF), solvent N-Methyl-2-pyrrolidone (NMP), nickel foam (Ni-foam), and carbon black (nanopowder) were obtained from Xiamen Tob Energy Technology, China. All the mentioned chemicals were of analytical reagent grade and were used without any further chemical modification (except aniline). Double distilled water was used to prepare all solutions.

Preparation of Ce-Doped PANI/Fe_3O_4 Nanocomposites

Magnetite nanoparticles were prepared by using the co-precipitation method (Ghandoor et al., 2012). The solutions of $(NH_4)_2Fe(SO_4)_2.6H_2O$ and $FeCl_3.6H_2O$ were mixed at a 1:2 ratio at 80°C, in an alkaline medium (0.8 M NaOH) to obtain Fe_3O_4 nanoparticles. Then, 1.82 ml of purified aniline was dispersed into 150 ml of 1.0 M HCl. Subsequently, 91.0 mg of $Ce(NO_3)_3.6H_2O$ was added to the solution and stirred at room temperature for 15 min to facilitate the proper dispersion of Ce^{3+} ions. An appropriate quantity of Fe_3O_4 nanoparticles (1, 3, 5, and 7 wt.%) and cetrimonium bromide (CTAB) in 20 ml of double distilled water was ultrasonicated for 20 min.

The mixture was dispersed with aniline and cerium nitrate by further ultrasonication for 30 min. Then, 2.0 g of $(NH_4)_2S_2O_8$ in 30 ml of 1.0 M HCl was dropped into the above solution slowly under constant stirring for 7 h to complete the polycondenzation polymerization process. The final products were collected by filtration, washed with distilled water and ethanol, and dried for 16 h at 70°C. Also, for comparison, pure PANI and Ce-doped PANI were synthesized in the same manner without the addition of Fe_3O_4 nanoparticles and CTAB (Ghandoor et al., 2012).

Characterization of Synthesized Materials

The Fourier-transform infrared spectroscopy (FTIR) spectra of PANI and PANI/Ce with different wt.% of Fe_3O_4 were recorded using the IRPrestige-21 FTIR spectrometer (Shimadzu, Japan) in the range of 4,000–390 cm^{-1}. The crystalline phase of the materials was investigated by powder X-ray diffraction (XRD) measurements on a Bruker diffractometer (Billerica, MA, United States) using Cu-Kα radiation (λ = 1.5406 Å) in the range of 2θ = 10°-70°. The UV-Vis spectra of materials dispersed in NMP were recorded using the Specord 200 Plus spectrophotometer (Analytik Jena, Jena, Germany). The morphology of the materials was observed by field-emission scanning electron microscopy (FE-SEM; S7400, Hitachi, Japan) equipped with an energy dispersive x-ray spectrometer (EDX), and the structure was characterized by transmission electron microscopy (TEM; JEM-2200, JEOL, Japan; 200 kV).

Electrochemical Measurements

All electrochemical properties were evaluated in a three-electrode setup comprising of a platinum wire as a counter electrode and a saturated calomel electrode (SCE) as a reference electrode. A Hokuto Denko (Japan) Ha-151 Potentiostat/Galvanostat controlled by a self-made LabVIEW-based program (Neupane, 2013) was used for the electrochemical measurements. The working electrodes were prepared by pressing a homogeneous slurry formed by grinding 80 wt.% active materials, 10 wt.% PVDF, and 10 wt.% carbon black with a few drops of the NMP solvent. The composition was further fixed onto a nickel foam current collector with a dimension of 1.0 cm × 0.5 cm and dried in a vacuum oven at 60°C for 12 h. The loading mass of active materials for all electrodes was 3.0 mg. CV and GCD measurements were carried out to estimate the capacities and cyclic stability of the materials in 1.0 M H_2SO_4. The specific capacity (Csp) was calculated from the integration of the resulting cyclic voltammogram, according to the equation (Zhang and Pan, 2015; Chen, 2017; Iqbal et al., 2020a; Numan et al., 2020):

$$C_{sp} = \frac{\int_{E1}^{E2} IdU}{2 \times 3.6 \times m \times \nu} \quad (1)$$

The values of *Csp*, energy density (*E*), and power density (*P*) were calculated from GCD according to the equation (Zhang and Pan, 2015; Chen, 2017; Iqbal et al., 2020a; Numan et al., 2020):

$$C_{sp}\,(\mathrm{mAhg^{-1}}) = \frac{I \times \Delta t}{m \times 3.6} \quad (2)$$

$$E\,(Whkg^{-1}) = \frac{1}{8}\,Csp \times \Delta U \quad (3)$$

$$ESR = \frac{IR_{drop}}{2 \times I} \quad (4)$$

$$P\,(Wkg^{-1}) = \frac{E \times 3600}{\Delta t}. \quad (5)$$

A two-electrode symmetric cell system was also assembled to compare the performance metrics with the results obtained from the three-electrode cell in the 1.0 M H_2SO_4 electrolyte using a separator. The values of *Csp*, *E*, and *P* were calculated according to the equation (Zhang and Pan, 2015; Chen, 2017; Iqbal et al., 2020a; Numan et al., 2020):

$$C_{sp}\,(\mathrm{mAhg^{-1}}) = \frac{I \times \Delta t}{m \times 3.6}, \quad (6)$$

$$E\,(Whkg^{-1}) = \frac{1}{2}\,Csp \times \Delta U \quad (7)$$

$$P\,(Wkg^{-1}) = \frac{E \times 3600}{\Delta t}, \quad (8)$$

Where the equivalent series resistance *(ESR)* calculated from the IRdrop of GCD curve. The current *(I)* with a discharge time (Δt) between potential limits excluding IRdrop. The tested potential window (ΔU) and mass (m) of active material within the electrode is also calculated with the above equation. It is well-known that the specific capacity of a three-electrode cell is four times larger than that of a two-electrode cell, so for comparison, Equation (3) is divided by 4 (Zhang and Pan, 2015; Chen, 2017).

RESULTS AND DISCUSSION

Structure Characteristics and Morphology

The field-emission (FE-SEM) measurements were used to characterize the morphological features of different compositions. **Figure 1A** shows the aggregated coarse structure of the PANI nanorods. After doping Ce^{3+} on PANI, as shown in **Figure 1B**, well-distributed nanorods with nanopores are observed. The obtained morphology provides a large surface-area-to-volume ratio by averting the aggregation of PANI and may assist in influencing specific capacitance and charge–discharge rates. The SEM micrographs of Ce-doped PANI with different wt.% of Fe_3O_4 clearly show the short nanorod-like uniform morphological appearance (**Figures 1C–F**). Smooth Fe_3O_4 nanospheres are seen as adhered to the nanorods of PANI. The uniform morphology of the PANI/Ce+7 wt.% Fe_3O_4 composites exhibited extended interfaces with smaller particle size, as shown in **Figure 1F**. This feature might be due to the agglomerating tendency of the nanoparticles and the formation of a cluster or agglomerates.

From the SEM images, the effects of Ce doping and Fe_3O_4 addition on the morphological evolution of PANI nanocomposite helped to understand their role in developing a smaller particle size. For further structural information, PANI/Ce+5 wt.% Fe_3O_4

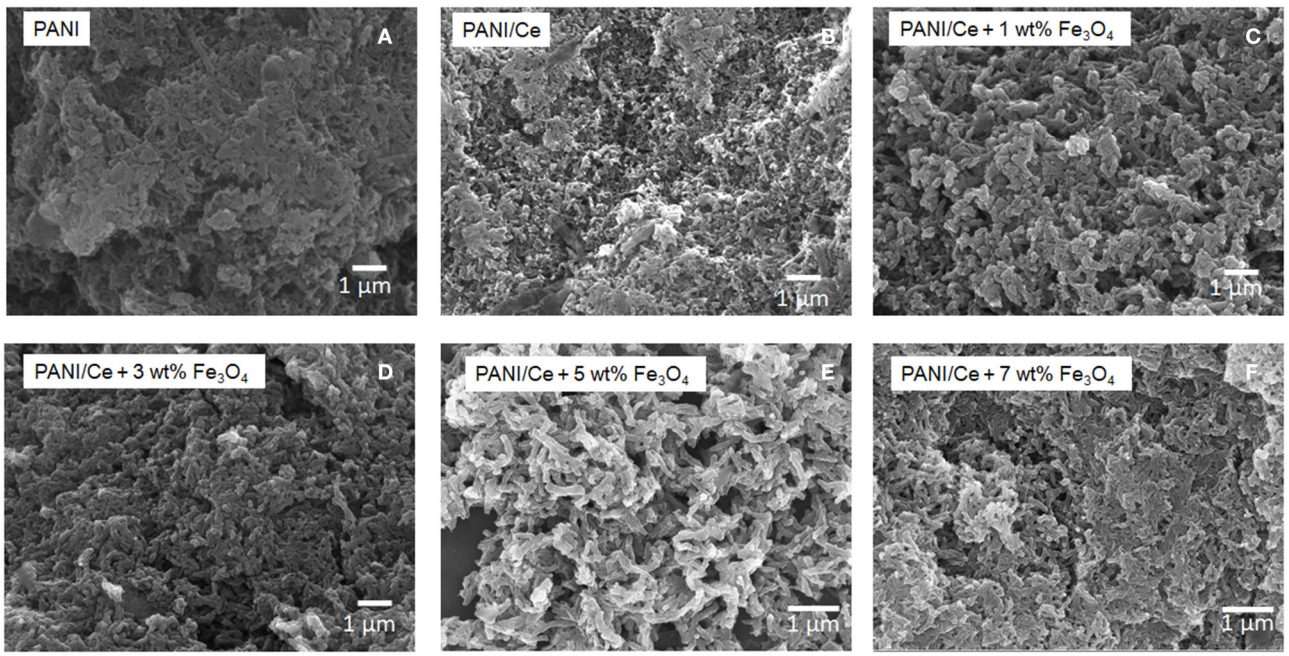

FIGURE 1 | SEM images of **(A)** PANI, **(B)** PANI/Ce, PANI/Ce with **(C)** 1 wt.%, **(D)** 3 wt.%, **(E)** 5 wt.%, and **(F)** 7 wt.% Fe_3O_4.

was chosen as the test subject to perform EDX mapping and TEM analysis. **Figure 2** represents the EDX mapping of the PANI/Ce+5 wt.% Fe_3O_4 with its elemental composition of C, O, N, and Ce. The elements are homogeneously distributed within the nanocomposite (**Figures 2A,B**).

The morphology and size distribution of the PANI/Ce+5 wt.% Fe_3O_4 nanocomposites were further analyzed using TEM. **Figure 3A** displays a short nanorod-like morphology. The image reveals that the PANI/Ce chain was absorbed on the surface of the Fe_3O_4 nanoparticles. The nanoparticles are uniformly dispersed in the PANI/Ce matrix and form a regular polymeric chain-like nanostructure. The average width is 50–60 nm, which was calculated by using the ImageJ software as presented in the histogram and Lorentzian curve fitting in **Figure 3B**. Also, the length of the nanorod is in the range of 150–200 nm (Li et al., 2009).

Figure 4 shows the FTIR spectra of PANI, PANI/Ce, and Ce-doped PANI with different wt.% of Fe_3O_4. The characteristic peaks at 1,590, 1,488, 1,294, 1,158, and 836 cm^{-1} are attributed to the C=C stretching mode of a quinonoid ring, C=C stretching mode of a benzenoid ring, C-N stretching mode of a quinonoid ring, C-H in-plane and out of plane bending mode of PANI, respectively (Butoi et al., 2017). The broadband around 3,435 cm^{-1} are allocated to the N-H stretching mode of PANI (Tharani and Vinayagam, 2015). The peak corresponding to N-H stretching at 3,435 cm^{-1} is broadened and less intense due to the simultaneous occurrence of another new vibrational mode after Ce-doping. Sharp absorption peaks at 518 and 452 cm^{-1} are assigned to the presence of Fe_3O_4 in the PANI/Ce matrix; however, PANI also shows firm peaks in the same regions; therefore, the peak intensity decreases with the increase in the amount of Fe_3O_4 (Silva et al., 2020).

Similarly, **Figure 5** represents the XRD patterns of Fe_3O_4, PANI, and PANI/Ce with different wt.% of Fe_3O_4. The diffraction peaks are associated with (111), (220), (311), (400), (511), and (440) planes, and all the Bragg planes are indexed to the cubic phase of Fe_3O_4 following the reported data (JCPDS file no. 79-0417) (Ghandoor et al., 2012). The average crystallite size of Fe_3O_4 nanoparticles is 8.45 nm, as calculated by using the Scherrer equation (Holzwarth and Gibson, 2011). Peaks that appeared at $2\theta = 15.2°$, 19.6°, and 26.1° revealed the semi-crystalline nature of PANI (Sampreeth et al., 2018). The degree of crystallinity of PANI/Ce with 3, 5, and 7 wt.% are found to be 2.16, 4.99, and 8.83%, respectively, as calculated using the (311) sharp peaks of Fe_3O_4 in the composites. In contrast, the XRD patterns of PANI/Ce with different wt.% of Fe_3O_4 displayed an increase in the degree of crystallinity with wt.% of Fe_3O_4 due to strong interaction between the vacant d-orbitals of Fe and the lone pair electrons of the nitrogen atom of PANI/Ce (Koysuren and Koysuren, 2019).

Figure 6A shows the UV-Vis spectra of PANI, PANI/Ce, and PANI/Ce with different wt.% Fe_3O_4. The observed absorption spectra revealed a significant absorption peak at 366 nm due to the Π-Π∗ transition of the benzenoid structure being in good agreement with the results mentioned in earlier work (Khan et al., 2015). A similar band is observed for PANI/Ce with the hypsochromic shift. And, the hyperchromic effect caused by a strong interaction between PANI and doped element, leading

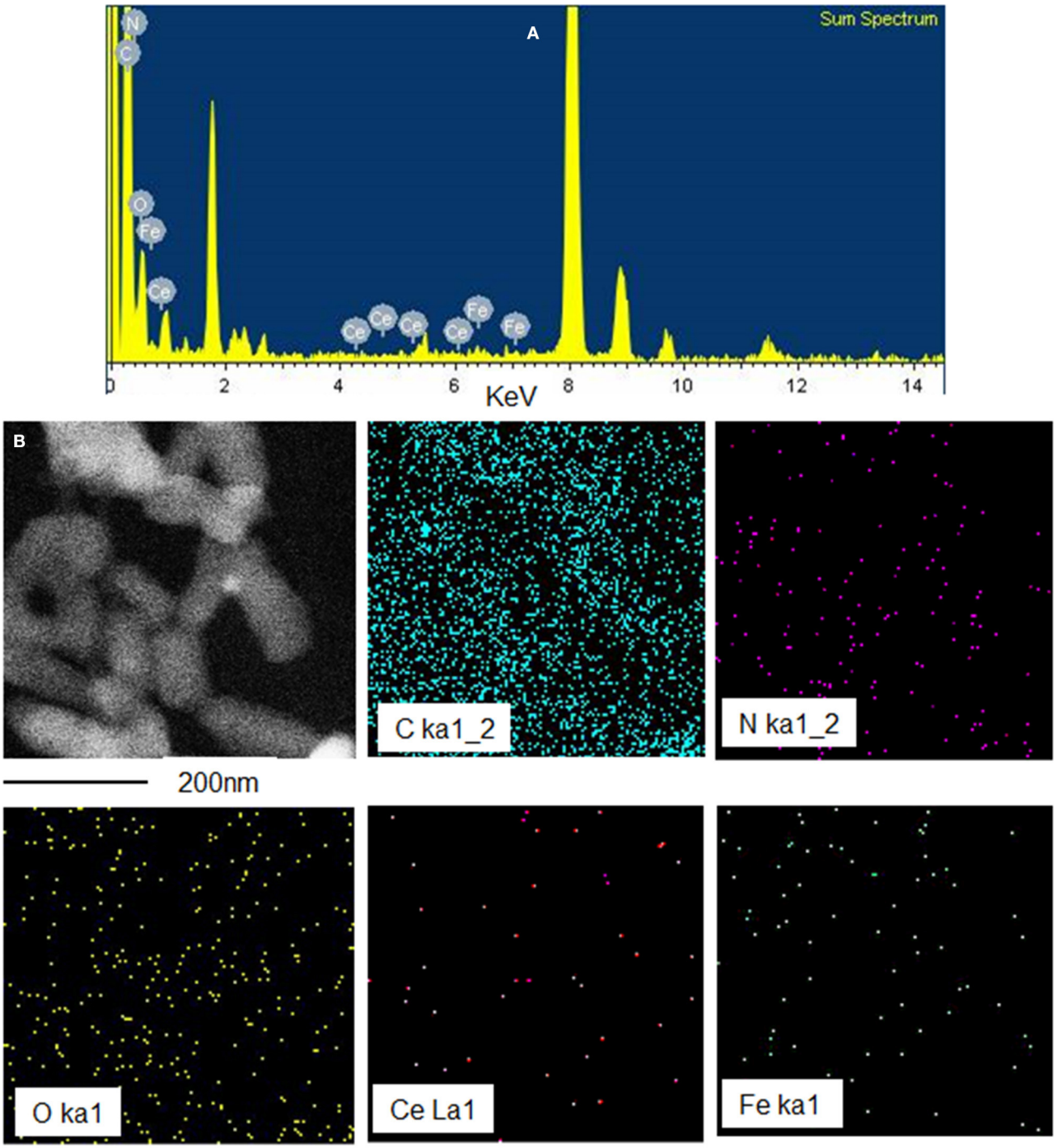

FIGURE 2 | (A) EDX patterns of PANI/Ce+5 wt.% Fe_3O_4, with the **(B)** corresponding elemental maps.

to an easy charge transfer process. A broad absorption band of Ce-doped PANI appears due to the superimposed electronic transition behavior on the other molecular energy state.

The UV-Vis spectra of PANI/Ce with different wt.% of Fe_3O_4 showed the hypochromic effect of Ce-doped PANI due to the strong interaction between the Fe_3O_4 nanoparticles and the Ce-doped polymer chain (Umare et al., 2010). Also, the hyperchromic effects are observed up to 5 wt.% of Fe_3O_4, and then the hypochromic effect was observed for 7 wt.% of Fe_3O_4. The uniform dispersion of Fe_3O_4 nanoparticles within the PANI/Ce matrix leads to higher broadness and intensity of the PANI/Ce+5 wt.% Fe_3O_4 nanocomposites. In PANI/Ce+7

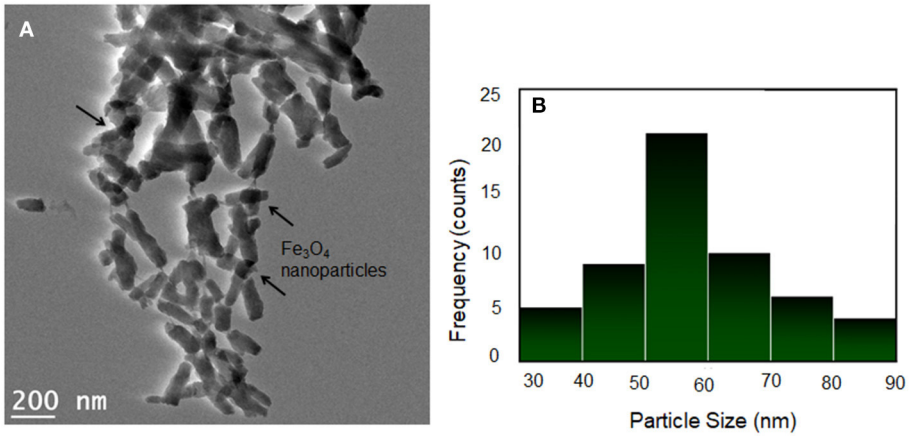

FIGURE 3 | (A) TEM image of PANI/Ce+5 wt.% Fe_3O_4 and **(B)** the corresponding histogram and Lorentzian curve fitting. The arrows denote Fe_3O_4 nanoparticles.

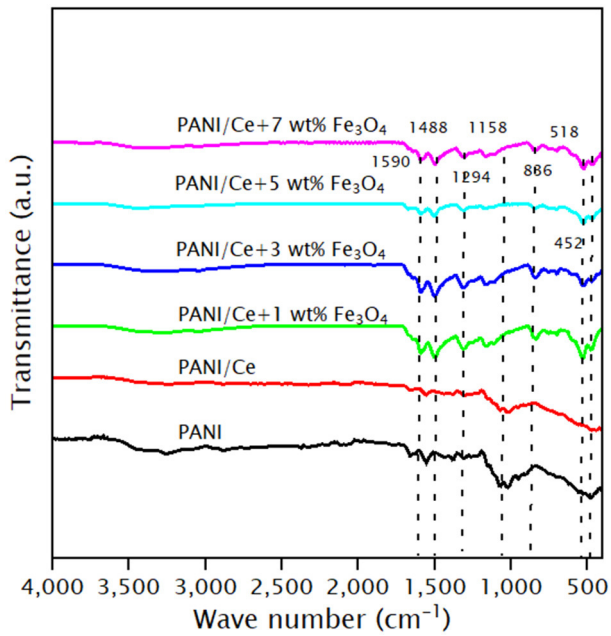

FIGURE 4 | FTIR spectra of PANI and PANI/Ce with 1, 3, 5, and 7 wt.% of Fe_3O_4.

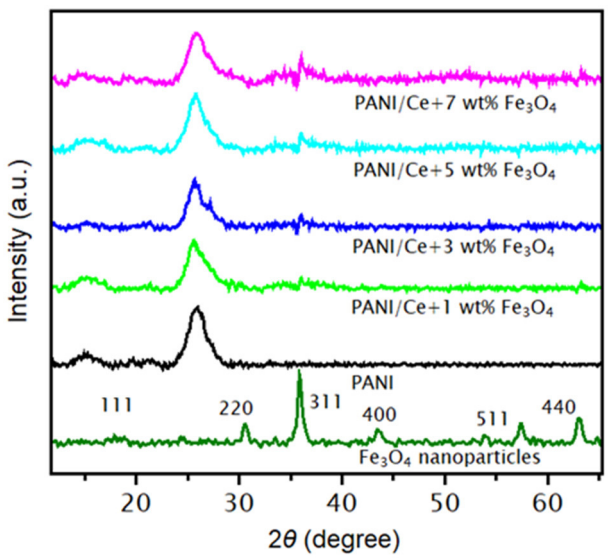

FIGURE 5 | XRD patterns of Fe_3O_4 nanoparticles, PANI, and PANI/Ce with 1, 3, 5, and 7 wt.% Fe_3O_4.

wt.% Fe_3O_4, the aggregation and the formation of the cluster in the PANI/Ce matrix diminished the intensity of the absorption peak. Therefore, it revealed a higher interfacial interaction for the 5 wt.% Fe_3O_4 composites (Sampreeth et al., 2018). Likewise, the bandgap energy of PANI, PANI/Ce, PANI/Ce+1, 3, 5, and 7 wt.% Fe_3O_4 were 2.78, 2.58, 2.63, 2.66, 2.70, and 2.73 eV, respectively (**Figure 6B**). The bandgap energy is decreased with Ce-doping, owing to allowed shallow states created in the bandgap (Bahmanrokh et al., 2020). Thus, the doping of cerium generated some energy levels that were close to the bandgap. It allowed a lower energy transition, resulting in a decrease in bandgap energy. Also, the bandgap energy increased with the wt.% of Fe_3O_4 in Ce-doped PANI due to the change in electron density and interfacial interactions (Sampreeth et al., 2018).

Electrochemical Characterizations

Electrochemical measurements were carried out to test the supercapattery performance of the prepared compositions. CVs of as-prepared PANI, PANI/Ce, and PANI/Ce with different wt.% of Fe_3O_4 used as the active electrode material in the three-electrode system were recorded at the sweep rate of 10 mVs^{-1}. The fixed operating potential range of −0.2 to 1.0 V vs. SCE in 1.0 M H_2SO_4 electrolyte was used. CVs of active materials show oxidation and reduction peaks due to the faradic charge transfer process in the electrode materials, as shown in **Figure 7A**. The CV of PANI was composed of two redox couple reactions. The

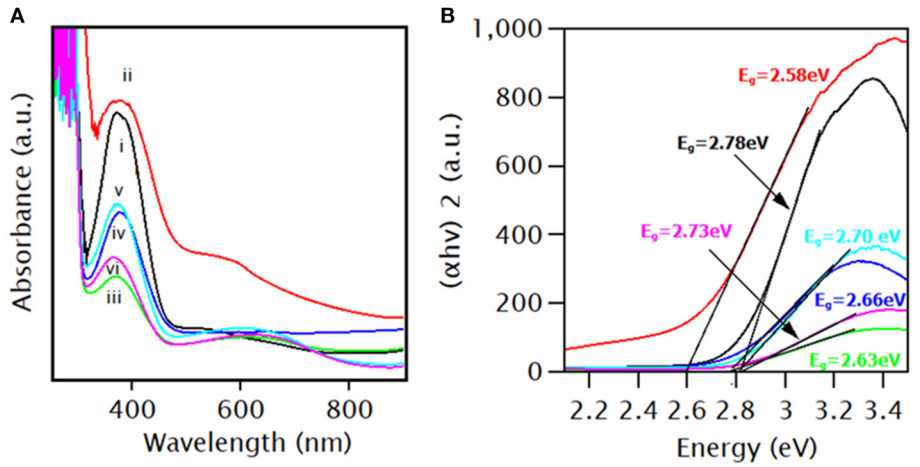

FIGURE 6 | (A) UV-Vis spectra of (i) PANI, (ii) PANI/Ce, PANI/Ce with (iii) 1 wt.%, (iv) 3 wt.%, (v) 5 wt.%, and (vi) 7 wt.% Fe_3O_4, and **(B)** the corresponding Tauc plot.

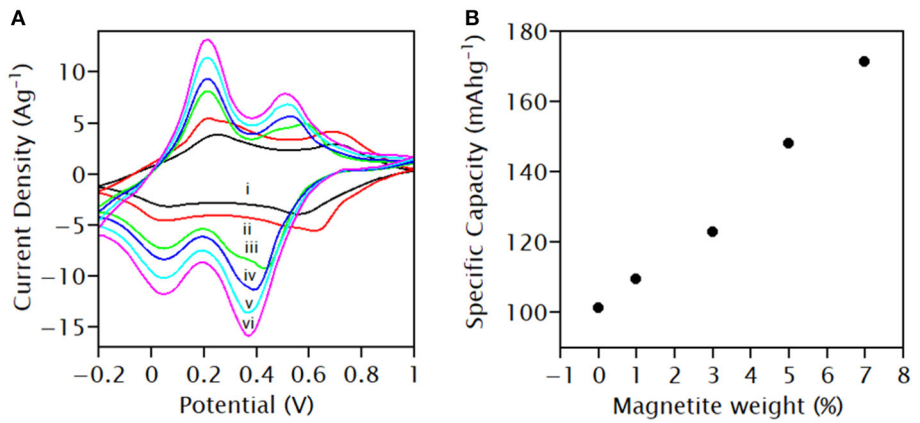

FIGURE 7 | (A) Cyclic voltammetry of (i) PANI, (ii) PANI/Ce, PANI/Ce with (iii) 1 wt.%, (iv) 3 wt.%, (v) 5 wt.%, and (vi) 7 wt.% Fe_3O_4 in the three-electrode system at a scan rate of 10 mVs^{-1}; **(B)** variation of specific capacity of PANI/Ce with wt.% of Fe_3O_4.

presence of an oxidization peak at about 0.23 V was due to the transformation of leucoemeraldine to conductive emeraldine salt form and the presence of another at 0.72 V was due to the formation of a fully oxidized pernigraniline state from the emeraldine oxidation state. The reduction peaks at 0.05 and 0.58 V represent the transformation of the leucoemeraldine and emeraldine base, respectively (Martyak et al., 2002). The Ce-doping led to a shift in oxidation peaks to 0.20 and 0.67 V, and the reduction peaks to 0.03 and 0.63 V, toward lower potential. As the wt.% of Fe_3O_4 increased in Ce-doped PANI, the peaks further shifted to the lower potential with an increase in the area of CV.

The formation of composites with Fe_3O_4 has enhanced the electrochemical performance of the Ce-doped PANI electrode due to three different redox mechanisms (Martyak et al., 2002). On the integration of the CV curves of PANI/Ce with 7 wt.% Fe_3O_4 from −0.2 to 0.0 V vs. SCE, a capacitance of 263.5 F/g was calculated due to capacitive charge storage. Also, the same calculation was performed on the same CV within the potential windows of −0.2 to 0.2 V, 0.2–0.4 V, and 0.4–0.8 V, and the capacitance values were calculated to be 1,071.5, 1,057.25, and 908.25 F/g, respectively, with a pair of redox peaks, which indicate that the capacitive charge storage mixed along with the faradic charge storage arises from a faradic mechanism involving peak-shaped CV. This calculation indicates that charge storage (Q) is some continuous function of the potential (U), and the derivative dQ/dU arises, which has properties of capacitive mentioned by Brousse et al. and non-capacitive faradic contribution (Brousse et al., 2015).

The specific capacity of PANI/Ce+7 wt.% Fe_3O_4 is 172 $mAhg^{-1}$ (616.8 Cg^{-1}), whereas that of pure PANI is 70 $mAhg^{-1}$ (252 Cg^{-1}). The specific capacity of Ce-doped PANI increased from 102 to 172 $mAhg^{-1}$ with an increment in the wt.% of Fe_3O_4 from 1 to 7 wt.%, as depicted in **Figure 7B**. The results might be due to the increasing exposure of the electrode surface and increasing the number of active sites for surface redox reaction with the formation of composites (Augustyn et al., 2014).

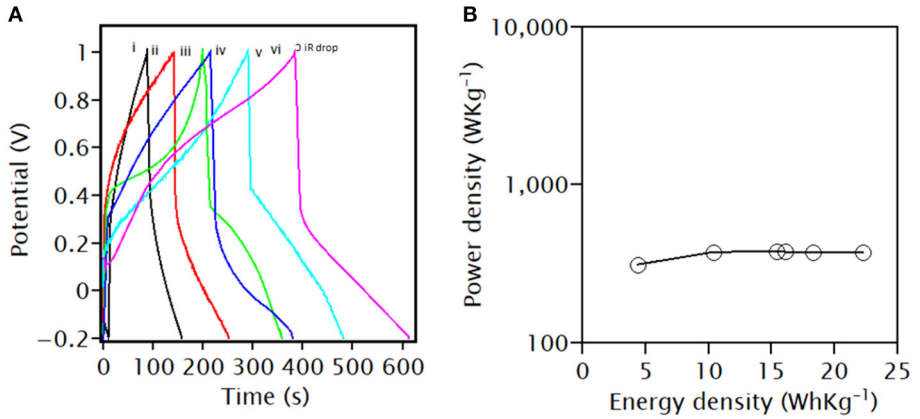

FIGURE 8 | (A) GCD plots of (i) PANI, (ii) PANI/Ce, PANI/Ce with (iii) 1 wt.%, (iv) 3 wt.%, (v) 5 wt.%, and (vi) 7 wt.% Fe_3O_4 in the three-electrode system at a constant current density of 2.5 Ag^{-1} and **(B)** the corresponding Ragone plot.

TABLE 1 | Specific capacity, energy density, and power density of prepared sample electrode calculated from GCD.

Samples	Specific capacity ($mAhg^{-1}$)	Energy density ($WhKg^{-1}$)	Power density (WKg^{-1})
Fe_3O_4	35	4.1	311.9
PANI	70	10.2	377.7
Ce doped PANI	103	15.2	381.2
1% Fe_3O_4	108	16.0	374.4
3% Fe_3O_4	122	18.0	374.8
5% Fe_3O_4	149	22.1	376.9
7% Fe_3O_4	171	25.4	376.6

Figure 8A shows the GCD curves of all the samples which were carried out at a current density of 2.5 Ag^{-1}. The GCD curves are non-linear and asymmetrical with charge–discharge plateaus, indicating that the capacity of PANI, PANI/Ce, and PANI/Ce with different wt.% of Fe_3O_4 mainly arose from both capacitive and non-capacitive contributions, as explained above (Iqbal et al., 2020a; Numan et al., 2020). A small IR drop in the GCD curve is observed (indicated by a linear drop). The specific capacity of PANI, Ce-doped PANI, and Ce-doped PANI with 1, 3, 5, and 7 wt.% Fe_3O_4 as a function of constant charge–discharge current density is found to be 70, 103, 108, 122, 149, and 171 $mAhg^{-1}$, respectively. These values are similar to the CV plot (**Figure 7A**). The performance metrics were calculated after deducing the IR drop, as shown in **Table 1**. The increase in the number of delocalized ions of PANI by doping of Ce improved the conductivity and enhanced the specific capacity in Ce-doped PANI (Li et al., 2018). Also, the pseudocapacitive contribution of the Fe_3O_4 nanoparticles increased the specific capacity of composites. Umare et al. reported a discharge capacity value of 78.8 $mAhg^{-1}$ at a current density of 0.5 $mAcm^{-2}$ from the GCD for Zn-PANI/Fe_3O_4 (9:1) (Umare et al., 2010). Furthermore, Iqbal et al. observed a discharge capacity value of 162.5 Cg^{-1} at a current density of 0.4 Ag^{-1} in MOF/PANI (50/50%) with the lowest ESR resistance (Iqbal et al., 2020a). When compared to this MOF/PANI electrode, the electrode presented in this paper exhibits a higher specific capacity, which may be due to the favorable microstructure for ion diffusion and enhanced conductivity.

However, the power density of the composite material value did not change significantly after 5 wt.% of Fe_3O_4 in the nanocomposites, as shown in **Table 1**. The result indicates that an increase in the wt.% of Fe_3O_4 nanoparticles above 7 wt.% would have enhanced the agglomerating tendency of nanoparticles. This would lead to the formation of clusters, which reduces the interfacial interaction between Fe_3O_4 and Ce-doped PANI, hence resulting in highly resistive electrode materials having lower power deliverance capacity.

As compared with the results from the other studies, the prepared PANI/Ce with 7 wt.% Fe_3O_4 offers a higher specific capacity of 171 $mAhg^{-1}$ at a current density of 2.5 Ag^{-1}. From the observation of the Ragone plot shown in **Figure 8B**, it can be seen that the PANI/Ce with 7 wt.% Fe_3O_4 composites display a maximum energy density of 25.4 $WhKg^{-1}$ (Equation 3) without compromising the high power density of 376.6 $WhKg^{-1}$ (Equation 4). **Table 2** gives a comparison of the results obtained in this study with the values of some other supercapattery electrode composite materials based on pseudocapacitive charge storage in aqueous electrolytes from other studies, which again shows that the material proposed in this study gives superior specific capacity values.

Figure 9 displays GCD profiles of PANI/Ce with 7 wt.% Fe_3O_4 at different current densities from 2 to 10 Ag^{-1}. The specific capacity decreases from 188.7 to 97.3 $mAhg^{-1}$ as the current density increases from 2 to 10 Ag^{-1}. The capacity value decreases by 91%. Similarly, the initial value decreases to 52% when the discharge current increases from 2 to 2.5 Ag^{-1} and 2 to 10 Ag^{-1}. The inner redox-active sites are not fully accessible for electroactive species at higher current densities, cause decreases in capacity value (Numan et al., 2020). The results indicate that the steady reversibility of the

electrode material results from a lower IR drop (Muthulakshmi et al., 2006). The inset shows the linear relation between the IR drop and current densities. A lower ESR value of 0.02891 Ω is found for the PANI/Ce with 7 wt.% Fe_3O_4, imparting a high charge–discharge ability of electrode materials. This lower value of ESR could be attributed to enhanced electrical conductivity that leads to rapid electron transport even at high current densities during the charge–discharge process (Padmanathan et al., 2016).

The symmetric supercapacitor with the supercapattery characteristics of PANI/Ce+5 wt.% Fe_3O_4 is further examined by GCD using a two-electrode system for device applications (**Figure 10**). The specific capacity, energy density, and power density are calculated to be 43 $mAhg^{-1}$ (Equation 5), 21.8 $WhKg^{-1}$ (Equation 6), and 374.9 WKg^{-1} (Equation 7), respectively. All the mentioned parameters are almost equal to the values calculated for the three-electrode system. It is worth noting that the specific capacity of the three-electrode system is almost four times the specific capacity of the two-electrode cell (Equation 2). This relates that the specific capacity of electrode materials is simply four-fold of the specific capacity of the cell in a symmetrical configuration (Chen, 2017). The results show a good capacity value shown by the nanocomposite of PANI/Ce+5 wt.% Fe_3O_4.

TABLE 2 | Comparative specific capacity performance of supercapattery electrodes based on pseudocapacitive charge storage in aqueous electrolytes.

S.N.	Electrode materials	Electrolyte	Potential window	Specific capacity ($mAhg^{-1}$)
1.	2D Co_3O_4 nanoflakes (Numan et al., 2020)	KOH (1 M)	0.0–0.4 V	30.2 (3 mVs^{-1})
2.	MOF/PANI (Iqbal et al., 2020b)	KOH (1 M)	0.0–0.6 V	45.0 (0.4 Ag^{-1})
3.	Sr_3P_2/PANI (Iqbal et al., 2020b)	KOH (1 M)	0.0–0.6 V	53.3 (3 mVs^{-1})
4.	NiS_2@NiV_2S_4 (Manikandan et al., 2019)	KOH (6 M)	0.0–1.6 V	144.4 (1.0 Ag^{-1})
5.	g-C_3N_4@$ZnCo_2O_4$ (Sharma and Gaur, 2020)	KOH (1 M)	0.0–0.4 V	154 (4 Ag^{-1})
6.	NiO-In_2O_3 Microflower 3D/Nanorod 1D (Padmanathan et al., 2016)	KOH (3 M)	−0.2 to 0.6 V	213 (5 Ag^{-1})
7	Ce-doped PANI/Fe_3O_4 nanocomposites [this study]	H_2SO_4 (1 M)	−0.2 to 1.0 V	171 (2.5 Ag^{-1})

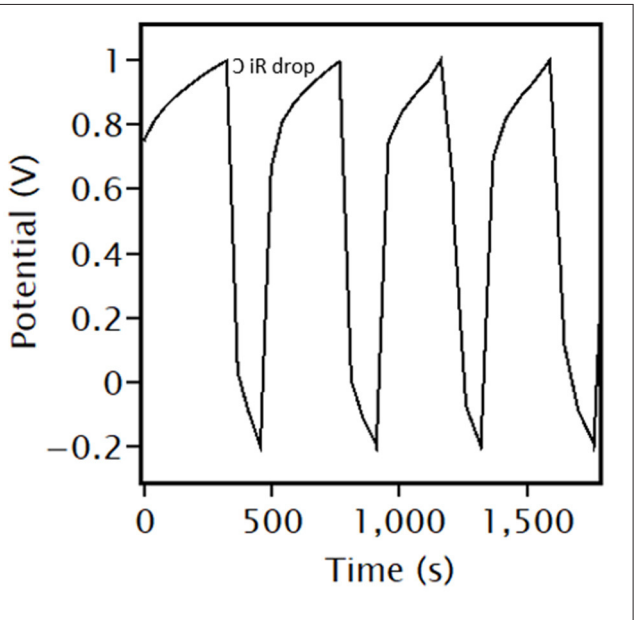

FIGURE 10 | PANI/Ce+5 wt.% Fe_3O_4 at the current density of 2.5 Ag^{-1} in the two-electrode system.

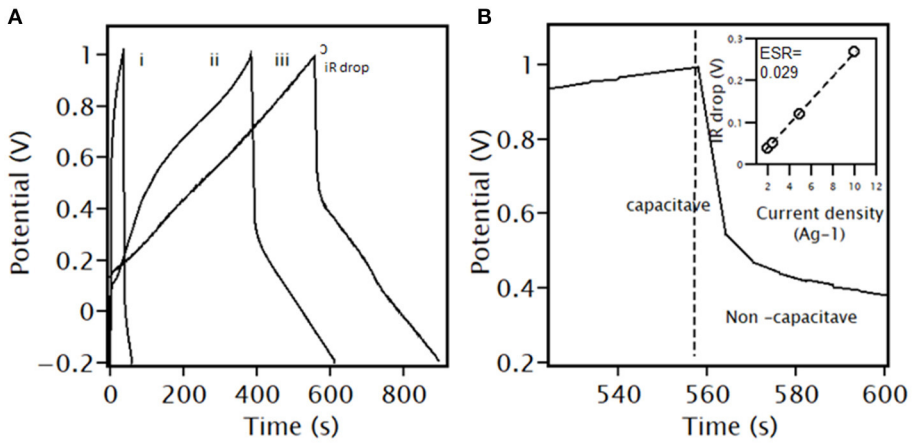

FIGURE 9 | GCD plot of PANI/Ce+7 wt.% Fe_3O_4 at different current densities of **(A)** (i) 10 Ag^{-1}, (ii) 2.5 Ag^{-1}, and, (iii) 2 Ag^{-1} in the three-electrode system; **(B)** Zoom-in of 2.5 Ag^{-1}. Inset: IR drop condition.

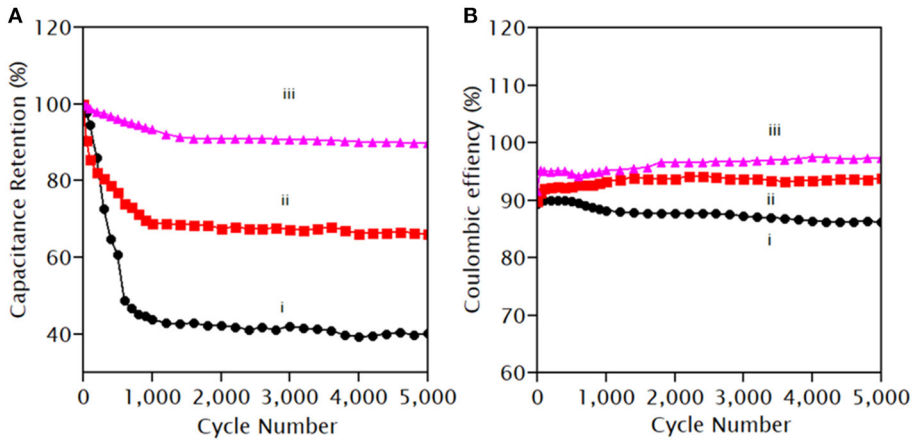

FIGURE 11 | (A) Cycling performance and **(B)** coulombic efficiency of (i) PANI, (ii) PANI/Ce, and (iii) PANI/Ce with 7 wt% Fe_3O_4.

The cyclic stability test showed that PANI retained 40% of the initial capacity after 5,000 cycles of CV at a scan rate of 100 mVs^{-1} between −0.2 and 1.0 V, as shown in **Figure 11A**. The inferior stability of PANI resulted from the strain generated by the swelling and shrinkage during the doping–dedoping of charged ions during CV (Eftekhari et al., 2017). However, PANI/Ce and PANI/Ce+7 wt.% Fe_3O_4 maintained almost 66.0 and 96.0% of their initial capacity, respectively. The support of the Fe_3O_4 nanoparticles in the composites can adapt to the volume change that helps to suppress the structural alternation and chemical degradation of PANI in the composite electrodes (Chen, 2017). The stability of iron oxides in an acidic medium has been extensively studied by Salmimies et al., who used nitric acid and sulfuric acid and found dissolution of magnetite at high enough concentrations of these acids (Salmimies et al., 2011). We have also found a 52% degradation of magnetite by the 1.0 M H_2SO_4 acid after 1,000 cycles of CV at 10 mV/s when used independently. However, the composite materials of PANI/Ce+7 wt.% Fe_3O_4 showed degradation of only 4%, and therefore, the composite was not affected by the stability of the individual component.

Also, the Coulombic efficiency of PANI, PANI/Ce, and PANI/Ce with 7 wt.% Fe_3O_4 was calculated to be 86.0, 93.8, and 97.3%, respectively, after 5,000 cycles, as shown in **Figure 11B**. The excellent stability over 5,000 cycles with retention of almost 96% of the initial capacity might be ascribed to the activation process which allows the trapped cations to diffuse out gradually or the insufficient contact of the nanocomposites with the H_2SO_4 aqueous solution during electrochemical processes (Gul et al., 2019). Thus, cyclic performance and Coulombic efficiency are enhanced due to the contribution of Ce and Fe_3O_4 on PANI and the synergistic interactions between them.

The enhanced electrochemical performance of PANI/Ce+7 wt.% Fe_3O_4-based supercapattery can be ascribed to (a) the multiple oxidation states of the redox-active electrode materials leading to the improved energy storage capacity of materials (Martyak et al., 2002); (b) the coordination effect between Ce and the N atom of PANI enhancing the conductivity of PANI, which gives fast accessibility for proton diffusion to electrochemically active sites (Li et al., 2018); (c) the composite formation of PANI/Ce with the Fe_3O_4 nanocomposites suppressing the mechanical stress, which leads to the enhancement in cyclability (Prasankumar et al., 2018); and (d) the high ionic conductivity of H^+ electrolyte promoting better redox reaction of the composites (Yuan et al., 2008).

CONCLUSION

This study introduces a simple and effective method to synthesize cost-effective and efficient supercapattery electrode materials. The specific capacity and power performances are greatly enhanced by the doping of Ce, followed by the incorporation of Fe_3O_4 in PANI. PANI/Ce exhibits a maximum capacity of 171 $mAhg^{-1}$ with an energy density of 25.4 $WhKg^{-1}$ and a power density of 376.6 WKg^{-1} with 7 wt.% Fe_3O_4 at 2.5 Ag^{-1} of load. The capacity retention is 96.0% after 5,000 cycles of charge–discharge. The synthesized composite is a promising candidate for supercapattery with its attributes of high specific capacities, power density, energy density, and cycle life.

DATA AVAILABILITY STATEMENT

The original contributions presented in the study are included in the article/supplementary material, further inquiries can be directed to the corresponding author/s.

AUTHOR CONTRIBUTIONS

SP and DG performed the experiments. AD, NK, SS, and RY helped to analyze the data. SP and SN provided the first draft

of the manuscript. AY conceived and designed the experiments. SN and AY finalized the manuscript. All authors analyzed the data, discussed the results, co-wrote the paper, and commented on the manuscript.

FUNDING

This project was funded by the University Grants Commission, Sanothimi, Nepal (University faculty research Grant No. FRG-73/74-S&T-08).

ACKNOWLEDGMENTS

The University Grants Commission, Sanothimi, Nepal was greatly acknowledged for providing the faculty research grant (Grant No. FRG-73/74-S&T-08). The Central Department of Chemistry and Tri-Chandra Multiple Campus, Tribhuvan University, Nepal, are thanked for providing all the necessary laboratory and instrumentation facilities (FTIR and UV-Vis). We would also like to thank the staff at the Center for Chonbuk University Research Facility (CURF), South Korea, for helping with the FE-SEM, EDS, and TEM analyses.

REFERENCES

Augustyn, V., Simon, P., and Dunn, B. (2014). Pseudocapacitive oxide materials for high-rate electrochemical energy storage. *Energy Environ. Sci.* 7, 1597–1614. doi: 10.1039/C3EE44164D

Bahmanrokh, G., Cazorla, C., Mofarah, S. S., Shahmiri, R., Yao, Y., Ismail, I., et al. (2020). Band gap engineering of Ce-doped anatase TiO_2 through solid solubility mechanisms and new defect equilibria formalism. *Nanoscale* 12, 4916–4934. doi: 10.1039/C9NR08604H

Ballarin, B., Boanini, E., Montalto, L., Mengucci, P., Nanni, D., Parise, C., et al. (2019). PANI/Au/Fe_3O_4 nanocomposite materials for high performance energy storage. *Electrochim. Acta* 322:134707. doi: 10.1016/j.electacta.2019.134707

Brousse, T., Bélanger, D., and Long, J. W. (2015). To be or not to be pseudocapacitive? *J. Electrochem. Soc.* 162:A5185. doi: 10.1149/2.0201505jes

Butoi, B., Groza, A., Dinca, P., Balan, A., and Barna, V. (2017). Morphological and structural analysis of polyaniline and poly(o-anisidine) layers generated in a DC glow discharge plasma by using an oblique angle electrode deposition configuration. *Polymers* 9:732. doi: 10.3390/polym9120732

Chen, G. Z. (2017). Supercapacitor and supercapattery as emerging electrochemical energy stores. *Int. Mater. Rev.* 62, 173–202. doi: 10.1080/09506608.2016.1240914

Eftekhari, A., Li, L., and Yang, Y. (2017). Polyaniline supercapacitors. *J. Power Sources* 347, 86–107. doi: 10.1016/j.jpowsour.2017.02.054

Ghandoor, H., El Zidan, H. M., Khalil, M. M. H., and Ismail, M. I. M. (2012). Synthesis and some physical properties of magnetite (Fe_3O_4) nanoparticles. *Int. J. Electrochem. Sci.* 7:12. Available online at: http://www.electrochemsci.org/papers/vol7/7065734.pdf

Gul, H., Shah, A.-H. A., and Bilal, S. (2019). Achieving ultrahigh cycling stability and extended potential window for supercapacitors through asymmetric combination of conductive polymer nanocomposite and activated carbon. *Polymers* 11:1678. doi: 10.3390/polym11101678

Hall, P. J., Mirzaeian, M., Fletcher, S. I., Sillars, F. B., Rennie, A. J. R., Shitta-Bey, G. O., et al. (2010). Energy storage in electrochemical capacitors: designing functional materials to improve performance. *Energy Environ. Sci.* 3, 1238–1251. doi: 10.1039/C0EE00004C

Holzwarth, U., and Gibson, N. (2011). The Scherrer equation versus the "Debye-Scherrer equation." *Nat. Nanotechnol.* 6:534. doi: 10.1038/nnano.2011.145

Hu, C., He, S., Jiang, S., Chen, S., and Hou, H. (2015). Natural source derived carbon paper supported conducting polymer nanowire arrays for high performance supercapacitors. *RSC Adv.* 5, 14441–14447. doi: 10.1039/C4RA12220H

Iqbal, M. Z., Faisal, M. M., Ali, S. R., and Alzaid, M. (2020a). A facile approach to investigate the charge storage mechanism of MOF/PANI based supercapattery devices. *Solid State Ionics* 354:115411. doi: 10.1016/j.ssi.2020.115411

Iqbal, M. Z., Faisal, M. M., Sulman, M., Ali, S. R., Afzal, A. M., Kamran, M. A., et al. (2020b). Capacitive and diffusive contribution in strontium phosphide-polyaniline based supercapattery. *J. Energy Storage* 29:101324. doi: 10.1016/j.est.2020.101324

Ji, H., Zhao, X., Qiao, Z., Jung, J., Zhu, Y., Lu, Y., et al. (2014). Capacitance of carbon-based electrical double-layer capacitors. *Nat. Commun.* 5:3317. doi: 10.1038/ncomms4317

Jiang, X., Setodoi, S., Fukumoto, S., Imae, I., Komaguchi, K., Yano, J., et al. (2014). An easy one-step electrosynthesis of graphene/polyaniline composites and electrochemical capacitor. *Carbon N. Y.* 67, 662–672. doi: 10.1016/j.carbon.2013.10.055

Khan, M. D. A., Akhtar, A., and Nabi, S. A. (2015). Investigation of the electrical conductivity and optical property of polyaniline-based nanocomposite and its application as an ethanol vapor sensor. *N. J. Chem.* 39, 3728–3735. doi: 10.1039/C4NJ02260B

Koysuren, O., and Koysuren, H. N. (2019). Photocatalytic activity of polyaniline/Fe-doped TiO_2 composites by *in situ* polymerization method. *J. Macromol. Sci. Part A* 56, 267–276. doi: 10.1080/10601325.2019.1565548

Li, H., Wang, J., Chu, Q., Wang, Z., Zhang, F., and Wang, S. (2009). Theoretical and experimental specific capacitance of polyaniline in sulfuric acid. *J. Power Sources* 190, 578–586. doi: 10.1016/j.jpowsour.2009.01.052

Li, Z., Shen, Y., Li, Y., Zheng, F., and Liu, L. (2018). Doping effects of cerium ion on structure and electrochemical properties of polyaniline. *Polym. Int.* 67, 121–126. doi: 10.1002/pi.5487

Ma, J., Liu, Y., Hu, Z., and Xu, Z. (2013). Electrochemical synthesis and performance of PANI electrode material for electrochemical capacitor. *Ionics* 19, 1405–1413. doi: 10.1007/s11581-013-0861-x

Manikandan, R., Raj, C. J., Yu, K. H., and Kim, B. C. (2019). Self-coupled nickel sulfide @ nickel vanadium sulfide nanostructure as a novel high capacity electrode material for supercapattery. *Appl. Surf. Sci.* 497, 143778. doi: 10.1016/j.apsusc.2019.143778

Martyak, N. M., McAndrew, P., McCaskie, J. E., and Dijon, J. (2002). Electrochemical polymerization of aniline from an oxalic acid medium. *Progr. Organic Coatings* 45, 23–32. doi: 10.1016/S0300-9440(02)00070-X

Muthulakshmi, B., Kalpana, D., Pitchumani, S., and Renganathan, N. G. (2006). Electrochemical deposition of polypyrrole for symmetric supercapacitors. *J. Power Sources* 158, 1533–1537. doi: 10.1016/j.jpowsour.2005.10.013

Neupane, S. (2013). *Development of a Window Based Program to Control the Analogue Potentiostat in Combination with an ADA Convertor*. Kathmandu: Journal of Nepal Chemical Society.

Nithya, V. D., and Arul, N. S. (2016). Progress and development of Fe_3O_4 electrodes for supercapacitors. *J. Mater. Chem. A* 4, 10767–10778. doi: 10.1039/C6TA02582J

Numan, A., Ramesh kumar, P., Khalid, M., Ramesh, S., Ramesh, K., Shamsudin, E. M., et al. (2020). Facile sonochemical synthesis of 2D porous Co_3O_4 nanoflake for supercapattery. *J. Alloys Compd.* 819:153019. doi: 10.1016/j.jallcom.2019.153019

Padmanathan, N., Shao, H., McNulty, D., O'Dwyer, C., and Razeeb, K. M. (2016). Hierarchical NiO-In_2O_3 microflower (3D)/ nanorod (1D) hetero-architecture as a high performance supercapacitor electrode with excellent cyclic stability. *J. Mater. Chem. A* 4, 4820–4830. doi: 10.1039/C5TA10407F

Patil, D. S., Shaikh, J. S., Dalavi, D. S., Karanjkar, M. M., Devan, R. S., Ma, Y. R., et al. (2011). An Mn doped polyaniline electrode for electrochemical supercapacitor. *J. Electrochem. Soc.* 158:A653. doi: 10.1149/1.3561428

Patil, D. S., Shaikh, J. S., Pawar, S. A., Devan, R. S., Ma, Y. R., Moholkar, A. V., et al. (2012). Investigations on silver/polyaniline electrodes for electrochemical supercapacitors. *Phys. Chem. Chem. Phys.* 14, 11886–11895. doi: 10.1039/C2CP41757J

Prasankumar, T., Wiston, B. R., Gautam, C. R., Ilangovan, R., and Jose, S. P. (2018). Synthesis and enhanced electrochemical performance of PANI/Fe_3O_4 nanocomposites as supercapacitor electrode. *J. Alloys Compd.* 757, 466–475. doi: 10.1016/j.jallcom.2018.05.108

Rantho, M. N., Madito, M. J., and Manyala, N. (2018). Symmetric supercapacitor with supercapattery behavior based on carbonized iron cations adsorbed onto polyaniline. *Electrochim. Acta* 262, 82–96. doi: 10.1016/j.electacta.2018.01.001

Salanne, M., Rotenberg, B., Naoi, K., Kaneko, K., Taberna, P.-L., Grey, C. P., et al. (2016). Efficient storage mechanisms for building better supercapacitors. *Nat. Energy* 1:16070. doi: 10.1038/nenergy.2016.70

Salmimies, R., Mannila, M., Kallas, J., and Häkkinen, A. (2011). Acidic dissolution of magnetite: experimental study on the effects of acid concentration and temperature. *Clays Clay Miner.* 59, 136–146. doi: 10.1346/CCMN.2011.0590203

Sampreeth, T., Al-Maghrabi, M. A., Bahuleyan, B. K., and Ramesan, M. T. (2018). Synthesis, characterization, thermal properties, conductivity and sensor application study of polyaniline/cerium-doped titanium dioxide nanocomposites. *J. Mater. Sci.* 53, 591–603. doi: 10.1007/s10853-017-1505-8

Sharma, M., and Gaur, A. (2020). Designing of carbon nitride supported $ZnCo_2O_4$ hybrid electrode for high-performance energy storage applications. *Sci. Rep.* 10:2035. doi: 10.1038/s41598-020-58925-4

Silva, C. A. S., Silva, R. L. S. E., Figueiredo, A. T., de, Alves, V. N., Silva, C. A. S., Silva, R. L. S., et al. (2020). Magnetic solid-phase microextraction for lead detection in aqueous samples using magnetite nanoparticles. *J. Braz. Chem. Soc.* 31, 109–115. doi: 10.21577/0103-5053.20190134

Simon, P., and Gogotsi, Y. (2008). Materials for electrochemical capacitors. *Nat. Mater.* 7, 845–854. doi: 10.1038/nmat2297

Tharani, S., and Vinayagam, S. C. (2015). Synthesis and characterization of cerium oxide doped polyaniline/titanium oxide nanocomposites for supercapacitor applications. *Int. J. Inno. Res. Sci.* 4, 11213–11222. doi: 10.15680/IJIRSET.2015.0411066

Umare, S. S., Shambharkar, B. H., and Ningthoujam, R. S. (2010). Synthesis and characterization of polyaniline–Fe_3O_4 nanocomposite: electrical conductivity, magnetic, electrochemical studies. *Synth. Met.* 160, 1815–1821. doi: 10.1016/j.synthmet.2010.06.015

Wang, H., Zhenyu, G., Suwei, Y., Zixuan, L., and Weiguo, Z. (2017). Design and synthesis of ternary graphene/polyaniline/Co_3O_4 hierarchical nanocomposites for supercapacitors. *Int. J. Electrochem. Sci.* 12, 3721–3731. doi: 10.20964/2017.05.66

Xavier, C. S., Paskocimas, C. A., Motta, F. V., da Araújo, V. D., Aragón, M. J., Tirado, J. L., et al. (2014). Microwave-assisted hydrothermal synthesis of magnetite nanoparticles with potential use as anode in lithium ion batteries. *Mater. Res.* 17, 1065–1070. doi: 10.1590/1516-1439.264714

Yu, L., and Chen, G. Z. (2016). Redox electrode materials for supercapatteries. *J. Power Sources* 326, 604–612. doi: 10.1016/j.jpowsour.2016.04.095

Yu, L., and Chen, G. Z. (2020). Supercapatteries as high-performance electrochemical energy storage devices. *Electrochem. Energy Rev.* 3, 271–285. doi: 10.1007/s41918-020-00063-6

Yuan, C., Su, L., Gao, B., and Zhang, X. (2008). Enhanced electrochemical stability and charge storage of MnO_2/carbon nanotubes composite modified by polyanilinne coating layer in acidic electrolytes. *Electrochim. Acta* 53, 7039–7047. doi: 10.1016/j.electacta.2008.05.037

Zeng, G., Chen, Y., Chen, L., Xiong, P., and Wei, M. (2016). Hierarchical cerium oxide derived from metal-organic frameworks for high performance supercapacitor electrodes. *Electrochim. Acta* 222, 773–780. doi: 10.1016/j.electacta.2016.11.035

Zhang, S., and Pan, N. (2015). Supercapacitors performance evaluation. *Adv. Energy Mater.* 5:1401401. doi: 10.1002/aenm.201401401

Conflict of Interest: The authors declare that the research was conducted in the absence of any commercial or financial relationships that could be construed as a potential conflict of interest.